Check for updates

An ambient-stable and stretchable ionic skin with multimodal sensation†

Binbin Ying, [ID] [ab] Qiyang Wu, [ID] [ab] Jianyu Li [ID] *[bc] and Xinyu Liu [ID] *[abd]

Skin serves as a physical and hygroscopic barrier to protect the inner body, and also contains sensory receptors to perceive environmental and mechanical stimuli. To recapitulate these salient features, hydrogel-based artificial skins have been developed. However, existing designs are constrained by limited functionality, low stability, and requirement of external power. Herein, a novel artificial ionic skin (AIskin) – an analog of the diode based on controlled ion mobility – is demonstrated with high toughness, stretchability, ambient stability and transparency. The AIskin consists of a bilayer of oppositely-charged, double-network hydrogel, and converts mechanical stimuli and humidity into signals of resistance, capacitance, open-circuit voltage (OCV), and short-circuit current (SCC), among which the OCV- and SCC-based sensing signals are self-generated. Its multimodal sensation is maintained in a wide range of relative humidities (13–85%). It is demonstrated for wearable strain-humidity sensing, human–machine interaction and walking energy harvesting. This work will open new avenues toward next-generation, skin-inspired wearable electronics.

New concepts

To bridge the gap between human skin and its artificial counterparts, hydrogel iontronics is emerging as a promising alternative to electronic artificial skins, as it better mimics the human skin in terms of mechanical properties and sensing principles (*i.e.*, sensing signals are transmitted through ions rather than electrons). Here, inspired by the salient features of human skin, we report a novel design of hydrogel iontronics for developing an artificial ionic skin (AIskin) with unprecedented properties. Different from existing designs of hydrogel iontronics with only conductive ionic hydrogels, the AIskin features diode-like electrical characteristics based on controlled ionic movements, which is an analog of transmembrane ion transport of neuron sensors in human skin. It shows high stretchability and toughness, high optical transparency and ambient stability. It can sense force, strain and humidity by transducing mechanical and chemical inputs into four types of electrical signals (*e.g.*, resistance, capacitance, open-circuit voltage and short-circuit current), among which the last two are self-generated without the need for an external power supply. We demonstrate the application of the AIskin to wearable strain-humidity sensing, human–machine interaction, and energy harvesting. Thanks to the combination of its unique mechanical properties and multimodal sensation, the AIskin could enable the development of next-generation artificial skins with improved functionality and human–machine integration, and thus stimulate the further growth of hydrogel iontronics as a complementary technology to existing wearable and stretchable electronics.

Introduction

Skin is the largest organ of the human body, serving as a physical and hygroscopic barrier to protect the inner body and control transepidermal water exchange, while containing signal sensors to perceive various environmental stimuli such as pressure, deformation, and temperature.[1–4] These functions are linked with salient features of the skin: highly deformable polymer networks to resist physical damage;[5] hygroscopic

compositions (*e.g.*, pyrrolidone carboxylic acid) to retain water;[6] a variety of sensory neurons (*e.g.*, mechanoreceptors, thermoreceptors, and pain receptors) powered by biological sources to transduce stimuli into controlled ion movements and propagation of action potentials (Fig. 1A).[3,7,8] To recapitulate these features for wearable electronics and healthcare applications, significant efforts have been made toward engineering electronic counterparts of the human skin (*i.e.*, electronic skin), leading to various design strategies involving electronic components, elastomeric substances or a combination thereof.[9–20] Despite their remarkable functionalities and applications that have been demonstrated, existing electronic skins differ from the native skin in terms of charge carriers (electrons *versus* ions in native skin), and the content and permeability of water,

[a] Department of Mechanical and Industrial Engineering, University of Toronto, 5 King's College Road, Toronto, Ontario, M5S 3G8, Canada

[b] Department of Mechanical Engineering, McGill University, 817 Sherbrooke Street West, Montreal, QC H3A 0C3, Canada

[c] Department of Biomedical Engineering, McGill University, 3775 rue University, Montreal, QC H3A 2B4, Canada. E-mail: jianyu.li@mcgill.ca

[d] Institute of Biomaterials and Biomedical Engineering, University of Toronto, 164 College Street, Toronto, ON M5S 3G9, Canada. E-mail: xyliu@mie.utoronto.ca

† Electronic supplementary information (ESI) available. See DOI: 10.1039/c9mh00715f
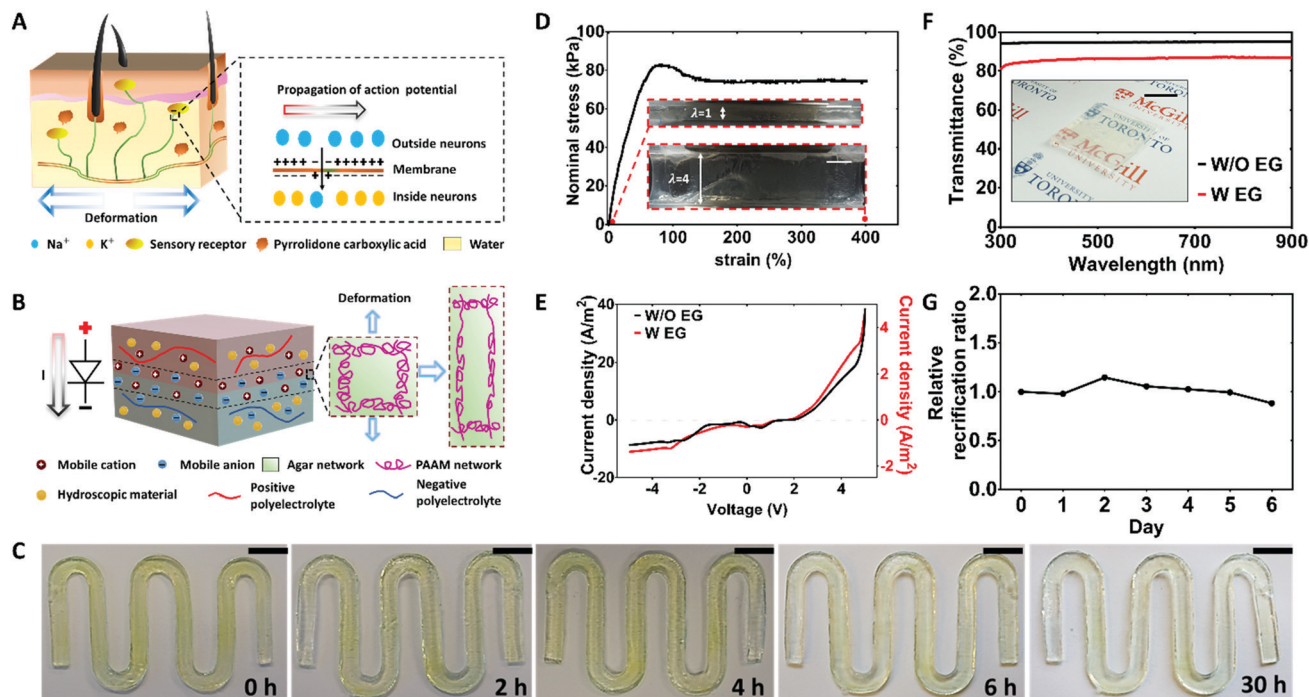
Fig. 1 Design and characterization of the AIskin. (A) Schematic of the human skin that resists physical damage, holds water due to the hygroscopic substance (*i.e.*, pyrrolidone carboxylic acid), and transports ionic signal directionally within sensory neurons. (B) Schematic illustration of the AIskin. The top layer is stretchable hydrogel containing positively-charged polyelectrolyte, and the bottom layer is stretchable hydrogel with the negative polyelectrolyte. The area between the two dashes indicates the depletion zone at the interface. (C) AIskin strips show no additional swelling after 30 hour desalination in DI water, scale bar = 1 cm. Yellow dye is added for visualization. (D) AIskin is stretched to more than 400% (down inset) of the original length (upper inset) without fracture; scale bar in the two insets is 10 mm. (E) The rectifying performance of AIskin with (W, red line) and without (W/O, black line) EG. Scan rate is 179 mV s^{-1}. (F) Transmittance of an AIskin with and without EG right after synthesis. The thickness of the AIskin is 3 mm. The inset shows a transparent AIskin. Scale bar is 20 mm. (G) Rectifying stability of an AIskin with EG at the RH of 65%.

resulting in limited biocompatibility and suboptimal human–machine interfaces especially for long-term usage.[21,22]

While the gap between real and electronic skins persists, recent progress of iontronics highlights the use of hydrated and ionic materials like hydrogels for making ionic devices (*i.e.*, pressure sensors[23,24] and touchpad[25]), capable of transducing mechanical stimuli into electrical signals such as capacitance or resistance. The existing ionic devices usually convert the applied touch, pressure, deformation or temperature into a change in their resistance or capacitance, the electrical readout of which requires a continuous power supply with voltages typically of 1–10 V[26] and power consumptions of up to 0.015 mW (*i.e.*, around 3 AA batteries per week).[24] Although stretchable batteries can be integrated with those ionic devices,[27] the requirement of external or on-chip power supplies still, to some extent, compromises long-term usage. Further development is needed toward a multifunctional self-powered ionic device. First, the devices should be equipped with self-generated power to mitigate the need of an external power supply for long-term use. Second, they need to enable the sensing of more than one stimulus like the human skin. In addition, the devices must be physically stable (*i.e.*, mitigating water loss) during operation and biocompatible when interfacing with the human body.

To meet the aforementioned requirements, we report a new design and method to make ionic devices, called artificial ionic skin (AIskin), capable of recapitulating the salient features of the human skin. The AIskin exhibits excellent skin-like mechanical deformability and ambient stability. It can sustain more than 400% strain without rupture and maintain its function after storage and 800 cycles of deformation. Different from the previous ionic devices consisting of homogeneous hydrogels and/or elastomer, our design utilizes a heterogeneous hydrogel of bilayer structure, which realizes controlled ion movements responsive to the mechanical deformation and humidity. This design resembles the conventional semiconductor diodes structurally and the sensory neurons in human skin in terms of stimuli sensing function. The AIskin converts both mechanical stimuli and humidity into four types of electrical signals: resistance, capacitance, open circuit voltage (OCV) and short circuit current (SCC), of which the latter two signals are self-generated without external power supply. These features of our AIskin potentially blur the boundary between humans and devices, and promise broad use ranging from wearable and implantable devices, to soft robotics and wound dressing capable of monitoring the local body motion and moisture of the wound bed.[28–30]

Results and discussion

Design of AIskin

The AIskin is a bilayer double-network hydrogel with hygroscopic substances and positively- and negatively-charged polyelectrolytes

in its two separate layers (Fig. 1B). A hygroscopic material was incorporated into the matrix to reduce the loss of water and achieve humidity sensing capability; ethylene glycol (EG) was used as it is a neutral hygroscopic reagent and expected to impact minimally on the controlled ionic movement in the AIskin. The model polyelectrolytes used here include poly(sodium 4-styrenesulfonate) (PSS) and poly(diallyl dimethylammonium chloride) (PDAC), which carry negative and positive charges fixed to their polymer chains, respectively. The hydrogel matrix is composed of an interpenetrating agarose–polyacrylamide (Agar–PAAm) network, and the selection of Agar and PAAm for constructing the double-network hydrogel was due to their confirmed biocompatibility and wide use in biomedicine.[31] Such matrix features a unique design, where two initially separate pieces of Agar hydrogel, containing PSS and PDAC respectively, are bonded together with a single interpenetrating PAAm network into a monolithic "diode-like" device (see details in Fig. S1 (ESI†) and the Materials and methods section). Compared with the previously demonstrated one-pot synthesis,[32] this method significantly reduces additional swelling of the AIskin in aqueous environments (Fig. 1C), making it possible to predefine the geometries of the Agar–PAAm hydrogel and the resulting devices. Agar, as the first network, confines the polyelectrolyte chains and only allows the movement of mobile ions; this enables the directional ion transmission. We hypothesized that this unique design could lead to diode-like electronic characteristics (*i.e.*, unidirectional ion movements resulting in an OCV between the two hydrogel layers), as well as superior stretchability and physical integrity (particularly strong bilayer bonding) of the heterogeneous device.

Mechanical properties of the AIskin

The mechanical performance of the AIskin was first evaluated. The pure-shear tests showed that the AIskin can be stretched to more than 400% of its initial length without rupture (Fig. 1D and Movie S1, ESI†), and the measured fracture energy (*i.e.*, toughness) was up to 1826 J m^{-2} (Fig. 1D and Fig. S2A, B, ESI†). Interestingly, unlike other double-network hydrogels reported previously,[32–34] the AIskin showed a characteristic elastic-nearly-plastic behavior, in which the stress plateau, 'yielding strength', was at 82 kPa and the critical strain was 100% (Fig. 1D). The transition can be attributed to the breakage of physical cross-links of the Agar network and the effective crack-bridging effect of the PAAm network. This feature indicates a superior energy dissipating capacity, which may limit the stress transfer to the underlying tissues when interfacing with the human body.[33] To verify this, cyclic tensile and compression tests were carried out; the testing results revealed a large hysteresis loop in the first loading–unloading cycle (Fig. S2C and D, ESI†), corresponding to the breakage of physical cross-links of the Agar network. Following the first cycle, the hydrogel became elastic due to the permanent cross-links of the PAAm network. To examine the integrity of the bilayer structure, we performed standard 180-degree peeling tests (Fig. S2E, ESI†). The fracture appeared at one open end of the hydrogel layer with PSS without any debonding at the interface observed. In addition, no debonding of the two hydrogel layers was observed during the compression

and tensile tests of the AIskin, indicating that the bilayer structure held strong structural integrity. The results confirmed that the AIskin is highly stretchable and tough, in addition to its intrinsic heterogeneity (required for the diode function) to be shown below. It will meet the mechanical requirements of wearable electronics given the maximum strain (∼55%) of human motion.[35]

Diode-like electrical properties of the AIskin

The electrical characteristics of the AIskin were then examined. Stainless steel electrodes (0.02 mm thick) were used in the tests. Fig. 1E illustrates the representative current–voltage curves of the AIskin resembling those of conventional semiconductor diodes. The device is ON under forward bias (offset voltage: 2 V, Fig. 1E), and OFF under reverse bias (<2 V). The results are consistent with the mechanisms proposed previously:[36,37] under negative potential, the current density in the backward direction is dramatically reduced compared to that in the forward direction; when the positive potential goes higher than 1.23 V to overcome barriers of electrode reaction, the redox reactions of water begin with H$^+$ and OH$^-$ produced on the positive and negative electrodes, respectively; with the applied potential increased beyond >2 V, more ions (*e.g.*, H$^+$ and OH$^-$) are created and diffuse across the charged polyelectrolyte layer continuously, leading to the formation of water at the interface and the substantial increase of current density. The critical voltage was also verified with hydrogels with single polyelectrolyte (either PSS or PDAC) in Fig. S3A (ESI†) where the current density increased upon a potential greater than 2 V. The minute non-zero current at zero potential can be explained by the charging and discharging effects within the diode junction capacitance and the electrical double layer (EDL) capacitance between the electrode and hydrogel when the voltage scans from +5 V to 0 V.[38,39] Further capacitance–voltage (*C–V*) testing confirmed the existence of the junction capacitance within the ionic diode, by showing an unsymmetrical *C–V* response of the AIskin and symmetrical *C–V* responses of the bilayer PSS Hydrogel and the bilayer PDAC hydrogel (Fig. S4A, ESI†). The AIskin also revealed a frequency-dependent *C–V* characteristic in the negative bias range (Fig. S4B, ESI†), which is typical for conventional electronic diodes.[40]

Similar to other material matrices consisting of oppositely-charged polyelectrolytes, our AIskin functions like a diode with a rectification ratio of ∼5 (Fig. 1E), which is primarily attributed to the presence of a depletion zone at the interface of the oppositely-charged hydrogel bilayers. There was a reduction of the rectification ratio when the sweeping rate increased beyond 277 mV s^{-1} (Fig. S3B and C, ESI†). This observation confirms that the diode current was caused by unidirectional movements of the mobile ions in the AIskin, rather than by other types of charge carriers.[41] The depletion zone is only accessible to selective ions (Na$^+$, H$^+$, OH$^-$, and Cl$^-$) under positive potentials, indicative of controlled ion movements within the AIskin. In contrast, no rectifying effect was observed on samples consisting of hydrogels with sole positively- or negatively-charged polyelectrolytes (Fig. S3A, ESI†). The controlled ion movement

resembles the selective ionic movement in sensory neurons in natural skins.

Ambient stability of the AIskin

We next examined the effect of a hygroscopic substance on the ambient stability of the AIskin. Concentrated salts such as lithium chloride and calcium chloride, used in previous studies,[42] are inapplicable here as they will overwhelm the desired charge distribution within the AIskin and result in loss of diode-like response. To select a suitable hygroscopic substance, we used two criteria: (i) it should have no impact on the controlled ion movements in the AIskin matrix; and (ii) it can maintain the rectifying performance of the AIskin. Two neutral hygroscopic substances, EG and glycerol, were tested. We first demonstrated that both materials did not alter the electrical characteristics of the AIskin. The AIskin exhibited a good rectifying effect right after the addition of EG (Fig. 1E) or glycerol (Fig. S3D, ESI†). We also examined the rectification stability of our AIskin over long-term exposure in air. After three days of exposure under ambient conditions of a laboratory environment (21 °C and relative humidity of 60–65%), the AIskin with EG maintained a higher current density and a smaller reduction of the rectification ratio than the one with glycerol (Fig. S3D–F, ESI†). In addition, we also quantified the effect of the EG concentration for device treatment on the device rectification ratio, and found that the AIskin treated with 50% (v/v) EG maintained the highest rectification ratio after three days of exposure under the same laboratory environment (Fig. S3G–I, ESI†). Therefore, the 50% (v/v) EG was selected as the hygroscopic material to construct the ambient stable AIskin. The hydrogels treated with 50% (v/v) EG also maintained high transparency (Fig. 1F) quantified by a transmittance of 81–87% in the range of 300–900 nm, slightly lower than that (95%) of the samples without the EG treatment (Fig. 1F). Higher transparency can be realized by reducing the thickness of AIskin if necessary (Fig. S5, ESI†).

To further study the ambient stability of the EG-laden AIskin, the rectification ratios and mass changes of the samples stored under different moisture conditions were tested over six days. No obvious decrease of the rectification ratio was observed on the samples stored at the relative humidity (RH) of 65% over six days (Fig. 1G). The corresponding sample mass dropped to 77% of its original mass in the first three days of storage, and then became relatively stable in the range of 67–73% of the original mass during day 3–6 (Fig. S6, ESI†). Notably, in extremely dry environments (RH = 13%), our EG-laden AIskin still retained 50% of its original mass over six days storage (Fig. S6, ESI†), and showed no significant difference of the rectification ratio compared with the ones stored at higher RHs such as 65% and 85% (Fig. S7A, ESI†). In contrast, the devices without EG lost both the water content and rectifying effect entirely at the RH of 13% (Fig. S6 and S7B, ESI†). The stability of other electrical output signals (e.g., OCV) of the AIskin over storage will be discussed in the following section. These observations indicate that the EG-laden AIskin can preserve its electronic diode function in a wide range of RHs and could serve as a relatively ambient-stable material for many applications where the device needs to maintain its electronic functions at different moisture conditions.

Strain sensing capability of the AIskin based on four types of output signal

The hydrogel-based ionic diode has been applied to energy harvesting from mechanical compressions by converting its compressive deformation into the change of built-in potential and the diffusion of free ions.[37] Therefore, we hypothesized that our AIskin can sense mechanical stimuli not only through changes of its resistance and capacitance but also through changes in its OCV and SCC. Next, we characterized the AIskin for strain sensing based on different types of output signal. After ensuring that diode-like electrical performance is repeatable for multiple current–voltage measurements on one device (Fig. S7C, ESI†), different compressive strains were applied along the thickness of the AIskin (in the range of 6–44%). The device still maintained its electrical characteristic of a diode with a slight increase of its rectification ratio (Fig. S7D and E, ESI†). This phenomenon can be explained by the fact that, with a compressive strain, the counterionic current carriers migrate a shorter distance to the opposite electrode with the decrease of the device thickness, leading to an increase in the conductivity of the forward-based diode in the forward direction. The conductivity of the backward-based diode is less dependent on the thickness of the AIskin due to the depletion zone with extremely low conductivity.[41]

Next, we demonstrate that the AIskin can serve as a strain sensor. Due to its unique electronic properties, the AIskin exhibits unprecedented strain-sensing capacity, i.e., it transforms mechanical stimuli into self-generated electrical signals (i.e., OCV and SSC), besides its conventional sensing modes (e.g., resistance- and capacitance-based sensing).

The response of resistance and capacitance resembles that of ionic conductors with homogeneous charge distribution (i.e., homogenous ionic conductors). Fig. 2A shows a resistance-strain calibration curve of the EG-laden AIskin, which was collected under a forward-bias voltage of 3 V. As the compressive strain increased from 10% to 50%, the resistance at the RH of 65% reduced from 20.23 kΩ to 4.54 kΩ. Under compression, the device thickness decreased and the device in-plane area increased due to the incompressibility of the AIskin material.[43] For the resistance-based strain sensing, our AIskin behaves like a homogeneous ionic conductor that detects mechanical strains based on geometry-change-induced resistance change. To confirm this, we compared gauge factors of our AIskin, a bilayer of pure PSS hydrogels, and a bilayer of pure PDAC hydrogels, and found comparable gauge factor values (Fig. S8, ESI†). The AIskin can also sense strain based on the change in capacitance. Fig. 2B shows that the device capacitance at the RH of 65% increased from 2.85 μF to 9.54 μF as the compressive strain increased from 10% to 50%. Under compression, besides the increase of the hydrogel–electrode contact area, the effective capacitance per area increases within the hydrogel–electrode interface (Fig. S9A, ESI†), which is based on the redistribution
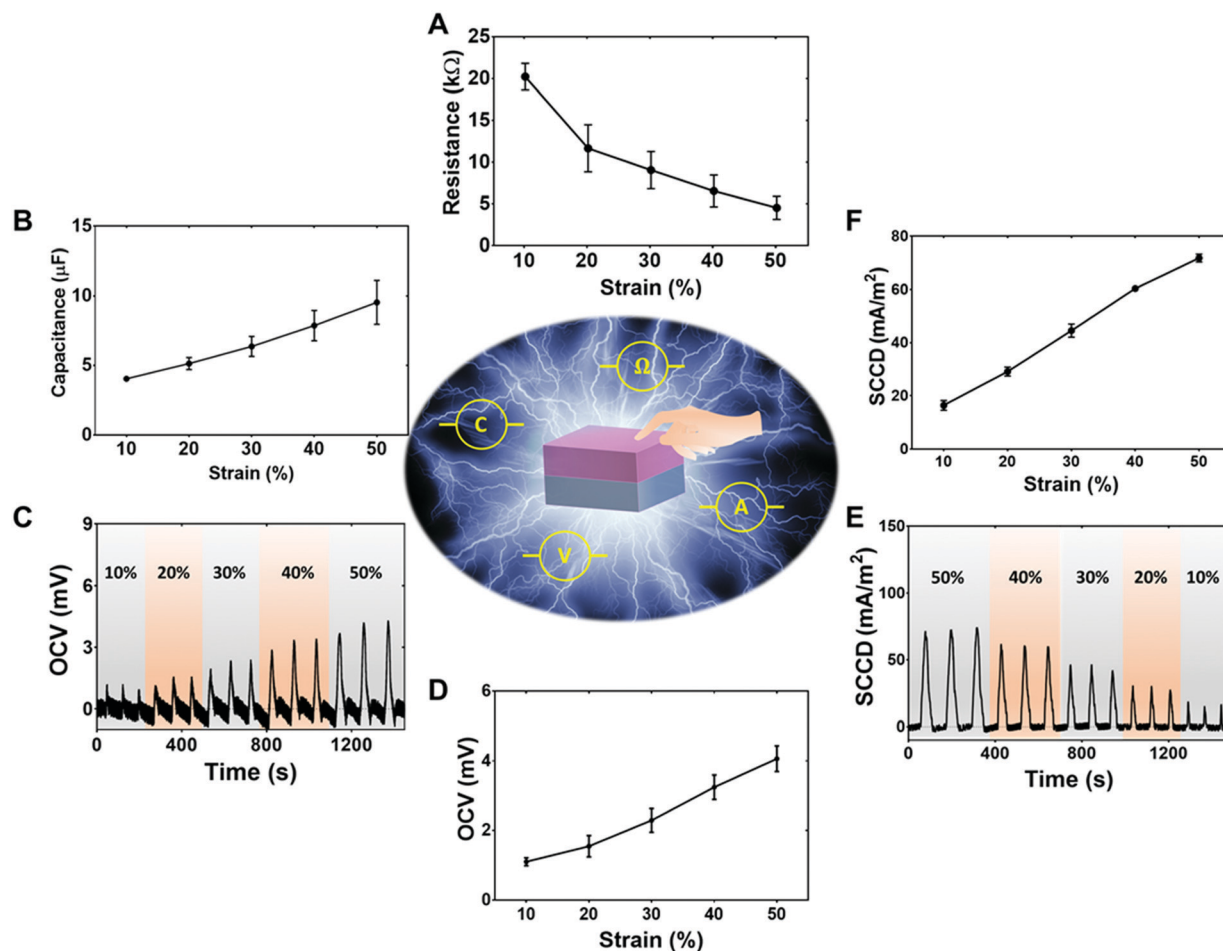
Fig. 2 Calibration of the EG-laden AIskin for strain sensing based on different output signals. (A) Calibration data of device resistance *vs.* strain at the RH of 65% (N = 3). (B) Calibration data of device capacitance *vs.* strain at the RH of 65% (N = 3). The compressive strains increase from 10% to 50%. (C) OCV output curves under repeated compression of different strain levels at the RH of 65%. The initial zero-strain OCV levels are adjusted to zero for comparison of the OCV peaks. The strain rising and reducing rates are 5 mm min^{-1} and 2.5 mm min^{-1}, respectively. (D) Calibration data of OCV peak *vs.* strain at the RH of 65% (N = 3). (E) SCCD output curves under repeated compression of different strain levels at the RH of 65%. The initial zero-strain SCCD levels are adjusted to zero for comparison of the SCCD peaks. The strain rising and reducing rates are 5 mm min^{-1} and 2.5 mm min^{-1}, respectively. (F) Calibration data of the SCCD peak *vs.* strain at the RH of 65% (N = 3). Error bars represent standard deviations.

of free ions and polyelectrolyte backbones within the EDL interfaces during deformation. We found no obvious difference of the capacitive gauge factor (GF$_c$) among the AIskin, PSS hydrogel bilayer, and PDAC hydrogel bilayer (Fig. S9B and C, ESI†), confirming that the capacitance change is predominantly due to the increase of capacitance in the EDL interface during compression.[38,44] These findings proved that our AIskin can be used for strain detection in wearable applications in the traditional resistance- and capacitance-based sensing modes.

In addition, our AIskin also allows for OCV- and SCC-based strain sensing without external power supply (*i.e.*, self-generated sensing modes). Ag/AgCl electrodes were used in these tests for collecting self-generated signals. We first measured the OCV output of our EG-laden AIskin under different compressive strain levels. Fig. 2C shows the measured waveforms of the device OCV with repetitive loads applied to compress the device to five different strain levels at the RH of 65%. From the curve at the strain of 50%, one can find that a potential increase followed

an applied strain, and that, once the load was removed, the mobile ion concentrations (thus the build-in potential) gradually recovered to their initial equilibria because of the elastic recovery of the hydrogel matrix. This strain-induced change in OCV can be explained as follows. The concentration gradients of mobile ions in the two hydrogel layers of our AIskin cause diffusion of Na$^+$ into the PDAC layer and Cl$^-$ into the PSS layer (Fig. 1 and Fig. S10, ESI†), a depletion region is formed at the interface of the two hydrogel layers. The geometry change of an AIskin under deformation can cause the re-diffusion of mobile ions and lead to a change of the device built-in potential (measured as the OCV), and larger deformation results in a larger OCV change. As the compressive strain increased from 10% to 50%, the peak of the OCV output (the built-in potential of the ionic diode) of the device increased from 1.1 mV to 4.1 mV (Fig. 2D). The OCV response to strain was much more obvious on the ionic-diode AIskin, than that on the PSS/PSS or the PDAC/PDAC hydrogel bilayers

(Fig. S11A, ESI†), suggesting that our diode-like AIskin can better realize self-generated, OCV-based strain sensing.

We then quantified the short circuit current density (SCCD) as a function of the compression strain. Fig. 2E shows the measured waveforms of the device SCCD with repetitive loads applied to compress the device to five different strain levels at the RH of 65%. Taking the data at the strain level of 50% as an example, a strengthened diffusion of ions was observed upon deformation, producing a large current pulse (average: 71.9 mA m^{-2}), which is comparable to that of an ionic system reported previously.[37] Moreover, thanks to the excellent mechanical property, the AIskin can produce longer current response time (the time duration of half peak SCCD response on strain) than those piezoelectric and triboelectric generators,[45–48] thus producing substantial energy with mechanical stimulus. Larger geometric deformation of an AIskin results in a larger SCCD. As the compressive strain increased from 10% to 50%, the peak value of SCCD increases from 16.5 mA m^{-2} to 71.9 mA m^{-2} (Fig. 2F). Any deformation-induced redistribution of the mobile ions can lead to a change of the SCCD in the material, and this phenomenon also exists on a bilayer of pure PSS/PSS or PDAC/PDAC hydrogel (Fig. S11B, ESI†).

In addition, the durability and performance stability of AIskin for strain sensing using self-generated signals were also tested. After ~800 cycles of repeated compressive loading–unloading cycles (16.7 h), the OCV change showed no noticeable degradation at the RH of 13% (Fig. S12A and B, ESI†), indicating good retention of the strain sensing function of the AIskin over repeated loading under dry environments. Besides, after one month of storage at the RH of 65%, the OCV output of the device showed only a slight decrease comparing to that of a device after 6 days of storage at the same RH value (Fig. S12C, ESI†).

To further test the strain sensing performance of our AIskin, we examined the robustness of the AIskin by measuring the four types of device outputs at different increasing speeds of the applied compressive strain. The resistance and capacitance outputs at the four deformation speeds are relatively stable [coefficient of variation (CV): 2% for resistance and 8.6% for capacitance] in the strain range of <50% (Fig. S13A and B, ESI†).
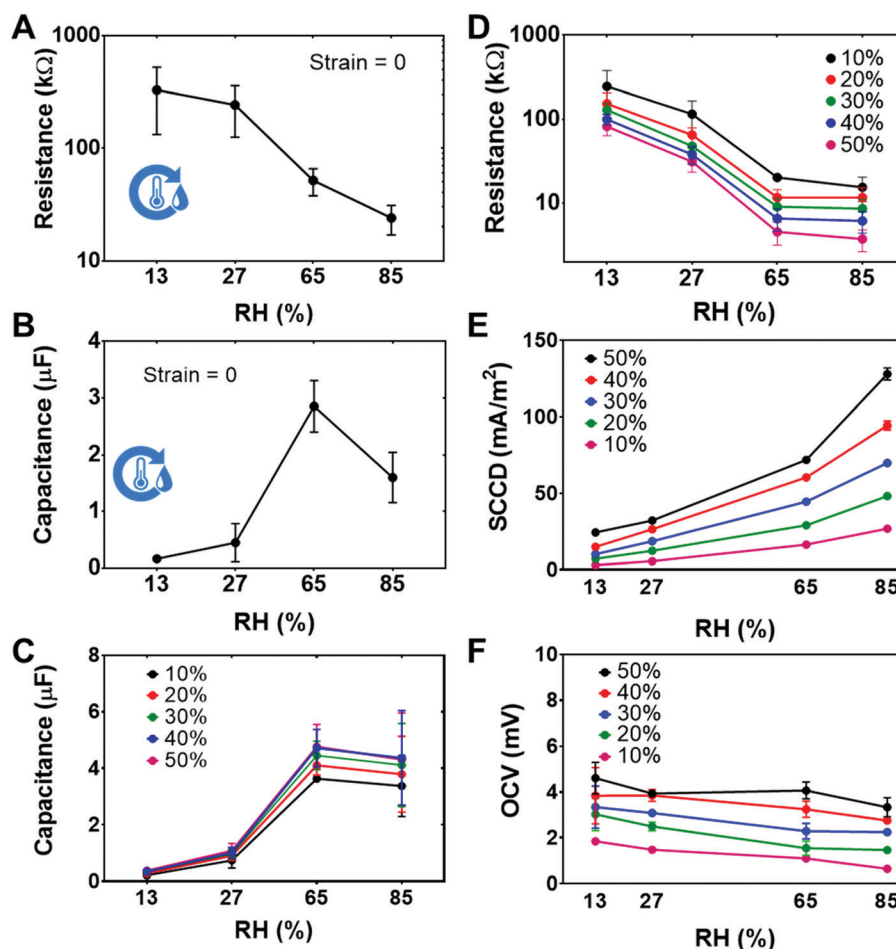

Fig. 3 Calibration of the EG-laden AIskin for humidity sensing based on different output signals. The RH increased from 13 to 85%. (A) Resistance–RH curve without strain (N = 3). (B) Capacitance–RH curve without strain (N = 3). (C) Capacitance–RH curves under different strain conditions (N = 3). (D) Resistance–RH curves under different strain conditions (N = 3). (E) SCCD–RH curves at different strain conditions (N = 3). (F) OCV–RH curves at different strain conditions (N = 3). Error bars represent standard deviations.

Similarly, the OCV and SCCD outputs also remained relatively constant (CV: 2% for OCV and 13% for SCCD) at the four strain rising speeds (Fig. S13C and D, ESI†). These data confirmed that our AIskin has repeatable strain sensing performance under different compressive loading conditions.

Humidity sensing capability of the AIskin based on four types of output signal

Besides strain sensing, we hypothesized that our EG-laden AIskin can be deployed as a humidity sensor, as the hydrated network can absorb or release water based on the ambient humidity, leading to changes in the ion concentration and distribution.[49] We conditioned the AIskin in an enclosed chamber of controllable relative humidity for 3 days to allow for sufficient water exchange, and measured the changes in its resistance and capacitance. We found that these signal outputs from the AIskin changed with the relative humidity (RH) of the environment (10–90%). As shown in Fig. 3A, without any strain applied, the device resistance decreased from 327 kΩ to 23.9 kΩ as the RH increased from 13% to 85%, indicating that

our AIskin can be used as a humidity sensor based on its resistance readout. In a drier environment, the water content inside the AIskin decreases, leading to a lower conductivity of the polyelectrolytes.[50] Under zero-strain conditions, the device capacitance increased substantially with the humidity in the RH range of <65%, and was then saturated at a higher RH level (Fig. 3B). This capacitance saturation phenomenon was further confirmed by the capacitance–RH data under different compressive strain levels (Fig. 3C). It can be understood that the number of dissociated ions and the ion mobility increase with the water content and RH, causing the increase of the effective capacitance within the EDL and depletion zone, and when the system is fully hydrated, this effective capacitance gets saturated.[50,51]

The response of the AIskin to both mechanical strain and humidity shows the potential of simultaneous strain and humidity sensing on the same monolithic device. We measured the capacitance, resistance, OCV, and SCCD of the AIskin under different strain levels at various humidity conditions (Fig. 3C–F). The results indicate that, when utilized as a humidity sensor
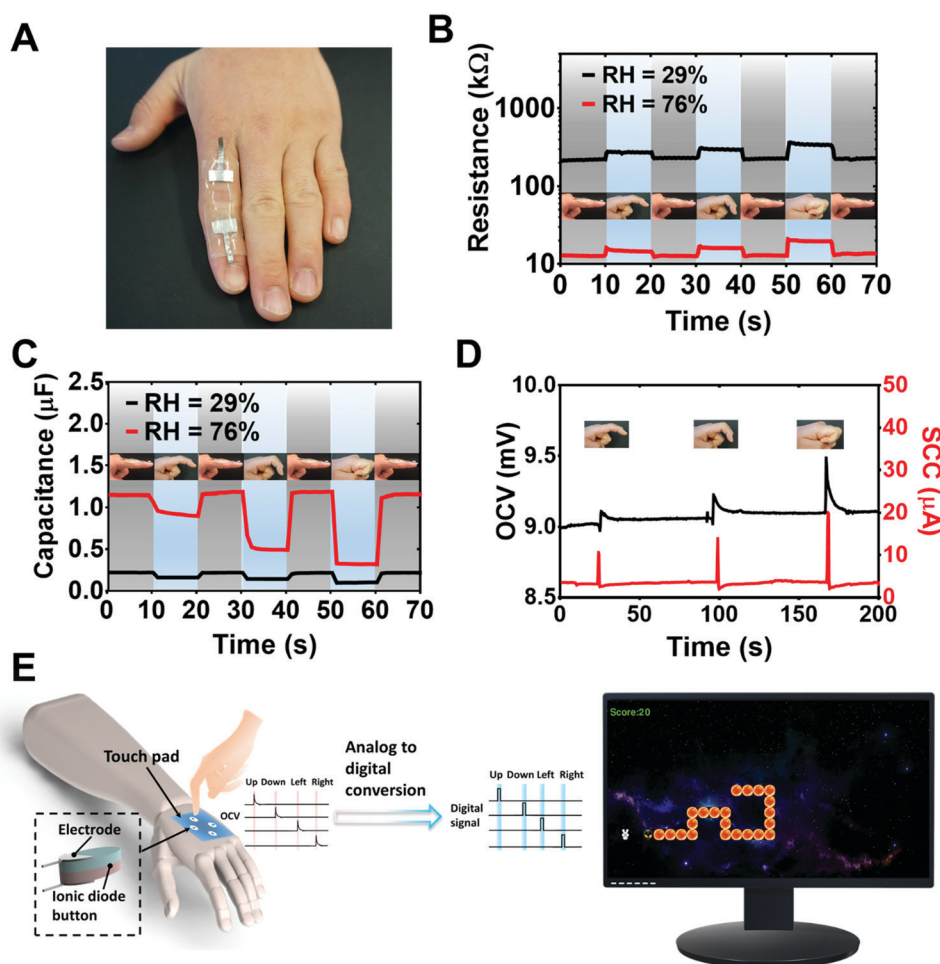

Fig. 4 Demonstrations of the AIskin as a wearable strain/humidity sensor and four-button artificial skin using self-generated signals for human–machine interaction. (A) An AIskin sensor mounted on an index finger for strain and humidity sensing. (B) Resistance and (C) capacitance outputs of the sensor at three different bending angles and two RH conditions. (D) SCC and OCV outputs at RH = 76%. (E) Schematic illustration of a four-button touch pad mounted on a human hand using self-generated signals to control the movement of a greedy snake by pressing the ionic diode buttons.
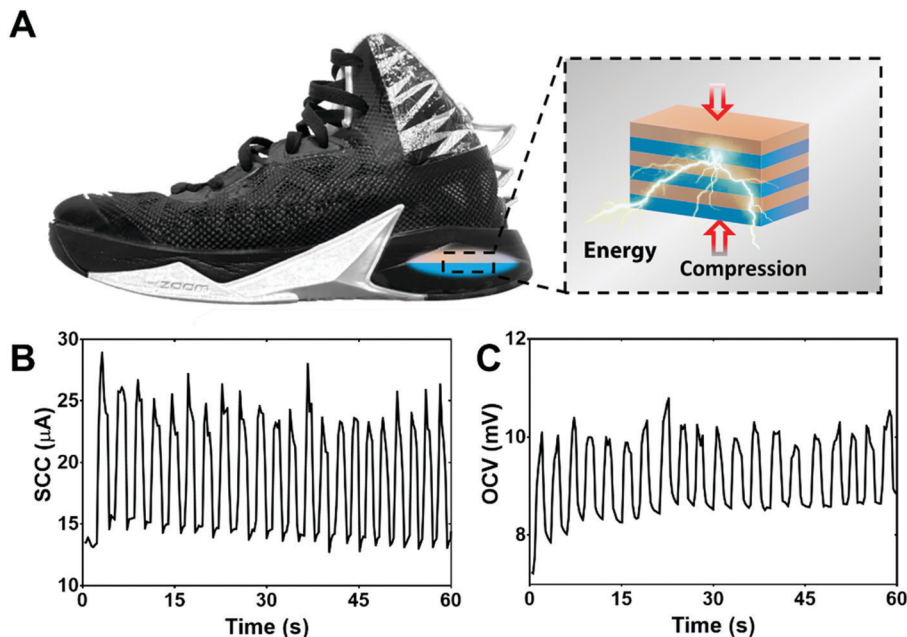
Fig. 5 Demonstration of the AIskin as a shoe walking energy harvester. (A) Schematic illustration of the mechanical walking energy harvesting. (B) SCC and (C) OCV outputs from an energy harvester inside a shoe heel; the step frequency is around 0.4 Hz.

under compressive strains, the resistance and SCCD sensing modes show more obvious changing trends with the RH change in the full RH range than the capacitance and OCV sensing modes. As the OCV outputs showed little correlation with the RH change, the SCCD mode is more suitable for humidity sensing.

Demonstrations of the AIskin

Thanks to the unique combination of its excellent mechanical and electrical performance, the AIskin can be used as a wearable sensor and an energy harvester. A wearable and stretchable finger joint strain sensor was constructed using the AIskin (Fig. 4A). The compliant sensor conformed to the surface of a finger joint during finger bending (Movie S2, ESI†), and detected the joint motion under different RH values of the environment. The finger's bending–straightening motions can be transduced into the change of resistance (Fig. 4B), capacitance (Fig. 4C), OCV and SCC (Fig. 4D). At different RH levels, the resistance and capacitance outputs of the device also changed (Fig. 4B and C), showing the feasibility of sensing

the environmental humidity using the same sensor. In addition, the strain sensing under the four sensing modes was rapid without obvious time delay in responding to the finger motion (Fig. 4B–D). The response and recovery time of the RH sensing were also measured in the resistance mode. An EG-laden AIskin with a thickness of 300 μm showed a faster performance of response time = 3 s and recovery time = 94 s than a commercial indoor digital hygrometer (B0778C8C9L, AMIR; response time: 30 s and recovery time 419 s; Fig. S14, ESI†). Faster response time of the RH sensing can be realized by reducing the thickness of the AIskin.[52]

We also constructed a four-button touch pad using self-generated signal (OCV-based), and employed it to play the video game, Greedy Snake, on a laptop computer (Fig. 4E and Movie S3, ESI†). This demonstration highlights the feasibility of using our AIskin as a human–machine interface.

Based on its self-generated sensing modes, the AIskin was also demonstrated for energy harvesting from human motions. We installed a piece of disk-shaped AIskin (diameter: 30 mm, and thickness: 8 mm) inside a shoe at its heel position (Fig. 5A),

Table 1 Comparison of energy harvesting performance between the AIskin and other devices reported previously

Peak SCCD (mA m^{-2})	Maximum strain	Energy output per stimulus^a (μJ m^{-2})	Frequency (Hz)	Working mechanism
128	Above 50%	3200	0.02–0.5^b	Ionic diode (this work)
7	0.03%	60	0.1^b	Ionic diode[54]
0.5	0.19%	0.12	11.2^c	Piezoelectric[55]
1.2	N/A	875	10–20^c	Triboelectric[46]
0.009	N/A	0.065	10–20^c	Triboelectric[45]
1.3	0.13%	585	10–20^c	Triboelectric[48]
14	N/A	703	10–20^c	Triboelectric[47]

^{a} Calculated as the product of half peak SCCD, half peak OCV and the time duration of half peak SCCD. ^{b} Calculated as strain rate divided by maximum strain. ^{c} Derived from the OCV–time curve.

and measured its OCV and SCC outputs (Fig. 5B and C) during walking. We calculated the power and energy output levels of our AIskin energy harvester based on the device calibration data (Fig. 3E and F). At a compressive strain of 50% and an RH of 85%, the peak SCCD and OCV produced by the AIskin are 128 mA m^{-2} (Fig. 3E) and 3.33 mV (Fig. 3F), respectively; hence, its maximum power output and average energy output were calculated to be 426.7 μW m^{-2} and 3200 μJ per mechanical stimulus, respectively. The average energy output of our device is larger than those reported previously (Table 1), showing the effectiveness of our AIskin material for low-frequency energy harvesting. The device power output can be further improved by assembling multiple thin layers of AIskin. The presented demonstrations show the great potential of our AIskin as a strain and humidity sensor using self-generated signals and/or a wearable low-frequency energy harvester, for applications such as human–machine interaction, wearable electronics, personal healthcare and beyond.

Conclusions

In this study, we reported a new design and method to fabricate diode-like bilayer DN hydrogels for ionic hydrogel devices (AIskin). The devices recapitulate the salient features of human skin by combining stretchability, ambient stability and sensing properties. Our results have demonstrated that the AIskin can sustain more than 400% strains without rupture, which is attributed to the double network design of the material, namely the synergistic effect of physically cross-linked agarose and covalently cross-linked PAAm networks. Importantly, the PAAm network enables seamless integration/adhesion of the two layers of preformed dissimilar hydrogels. The inclusion of neutral hygroscopic substance EG maintains the electrical characteristics of AIskin and substantially improves its stability in an ambient environment. Our results have also confirmed that AIskin is an ionic analog of the diode based on controlled movements of oppositely-charged ions at the interface of its bilayer structure. Compared to previously reported diode-like hydrogels made of brittle hydrogels, AIskin provides higher stretchability and toughness as well as ambient stability to resist water loss.

Thanks to the unique combination of mechanical, physical and electrical properties, the AIskin enables numerous applications such as strain/humidity sensing, human–machine interaction, and energy harvesting. We experimentally confirmed that the AIskin converts humidity and mechanical stimuli into changes in resistance, capacitance, OCV, and SCCD, and showed that the OCV- and SCCD-based sensing modes are self-generated due to the presence of an ionic diode structure, different from the widely used resistance- and capacitance-based sensing modes. In addition, we could also apply our AIskin design to ion sensing as external ionic stimuli have been proved to induce an amplified ionic current change within the ionic diode system.[53] In our current demonstrations, strain/humidity sensing are mainly conducted in an environment that does not induce obvious variations of the ion concentrations of the AIskin. Therefore, only mechanical and humidity stimuli need to be considered here. The AIskin can be calibrated for strain and humidity sensing in the four types of sensing modes. For proof-of-demonstration, a wearable finger joint sensor, a four-button touch pad using self-generated signals, and a shoe walking energy harvester were demonstrated for strain–humidity sensing, human–machine interfaces, and walking energy harvesting, respectively. Notably, in the energy harvesting demonstration, the energy output of our device is larger than some of the piezoelectric or triboelectric devices and non-stretchable ionic diodes (Table 1).[45–48,54,55] The power output can be further improved by assembling multiple layers of AIskin.

While this work was focused on the design, fabrication and characterization of the AIskin, further development is needed to increase the integration level and improve the performance of the AIskin. For instance, microfabrication methods for constructing micrometer-sized DN–hydrogel ionic diodes need to be developed to realize more complex AIskin systems such as wearable, self-powered micro-sensor arrays[56,57] and stretchable ionic logic circuits.[21,58] The resulting microscale ionic diode might have better electrical characteristics than the macroscopic counterparts because the scale-down of the depletion zone could enhance the rectifying performance of the AIskin.[41] Besides, microfabrication technology could enable a multi-functional sensor by integrating multiple pieces of AIskin on a single chip to decouple the AIskin's simultaneous response to both strain and humidity. For example, to monitor humidity and strain simultaneously, one can fabricate a monolithic AIskin device with one humidity sensor arranged on a body part without obvious deformation and another strain sensor on the body part with the maximum strains generated during operation. In this way, the strain sensor output can be compensated based on the environment humidity. One can also seal the strain sensor by a thin layer of elastomer[59] to reduce the coupling effect with humidity. To this end, one can resort to the existing manufacturing techniques such as soft lithography and 3D printing, which have been applied to the fabrication of stretchable electronics.[60–62] In addition, refining the electrical properties of the AIskin could improve the performance to meet the practical needs. For instance, the power output of AIskin against deformation can be improved by increasing the concentrations of the polyelectrolytes or doping the AIskin with high-conductivity material (e.g., CNTs).[37,41]

In summary, we developed an ambient-stable and stretchable ionic skin inspired by the salient features of human skin. It is a skin-like sensor with high stretchability and multifunctional sensing capability, and can serve as an alternative technology to current stretchable sensing and energy harvesting devices. The presented design and fabrication approach to construct mechanically-robust dissimilar hydrogel assemblies are applicable to other hydrogel systems. Given the diversity of polyelectrolytes and hydrogels, the repertoire of ionic devices could be expanded to achieve different functionalities, for instance, sensing of pH,[63] gas,[64] ion strengths[65] and glucose.[44,66] We envision that the design and method presented here will lead

to the development of next-generation wearable and implantable devices with improved human–machine interfaces.

Materials and methods

Materials

Poly(sodium 4-styrenesulfonate) solution (PSS, M_w = 70 kDa, 30 wt%), poly(diallyldimethylammonium chloride) solution (PDAC, M_w = 400–500 kDa, 20 wt%), agarose (biochemistry research grade), acrylamide (AAm), covalent cross-linker N,N′-methylenebis(acrylamide) (MBAA), photoinitiator IRGACURE 2959 (I2959), hygroscopic substances, ethylene glycol (EG), glycerol and humidity control reagent Lithium chloride (LiCl) were purchased from Sigma. Ag/AgCl ink was purchase from Ercon Inc. to fabricate a thin layer of electrodes (0.02 mm thick) on PET film. 3 M Very-High-Bond (VHB) foam tape (0.05 mm thick) were purchased from McMaster-Carr. Milli-Q (18.3 MΩ) water was used in all experiments.

Fabrication of artificial ionic skin (AIskin)

A facile two-step polymerization method was used to fabricate the AIskin (Fig. S1, ESI†). In the first step, the first network hydrogel with polyelectrolyte was synthesized following a previously reported protocol.[41] In brief, agarose (2.0 wt%) was added to PSS solutions (7.0 wt%) and PDAC solutions (5.0 wt%), respectively. The mixtures were heated at 100 °C for 20 min under continuous stirring to obtain a transparent pre-hydrogel solution. For gelation of the solutions, the hot mixtures were poured into glass molds and then cooled to room temperature for 20 min. In the second step, the PSS and PDAC gel were immersed in the degassed AAm precursor solution (17 wt%), containing 1 mM MBAA and 0.4 wt% I2959, for at least 12 h in the dark environment. Then, two layers of oppositely charged hydrogel containing AAm monomers were stacked together and clamped tightly in a glass mold. After that, the whole device was irradiated with 254 nm UV (28–32 mW cm^{-2}, UVO-Cleaner 42A, Jelight Company, Inc.) for 2 hours to cross-link the AAm monomers to form the second network. The obtained hydrogels were desalinated to remove residual ions (the desalination time is 4 hours unless indicated elsewhere) and then sealed in a Ziploc bag before tests. As a control, two layers of only positively or negatively charged DN hydrogel were synthesized respectively by the abovementioned method.

Fabrication and test of ambient stable AIskin

Hygroscopic reagents were added into the hydrogel devices to increase their ambient stability. The obtained DN hydrogel was immersed in the EG [25, 50 and 75% (v/v)] for at least 1 hour to reach the equilibrium state. 400 mL LiCl solution (19 M, 15 M, 8 M and 6 M) was stored in airtight plastic storage containers (86 oz.) to maintain a certain relative humidity (13%, 27%, 65%, and 85%, respectively). After the placement of EG processed devices, their mass and electric performance were monitored continuously for 1 week to evaluate the ambient stability. To compare the water retention capability of different hygroscopic reagents, glycerol solution (50 vol%) was also used in this test.

Mechanical characterization

Uniaxial compression tests were carried out with a rheometer (TA instruments). Cylindrical AIskin with a thickness of ∼4 mm and a diameter of ∼12 mm was utilized for compression tests. The compressive strain was estimated as t/t_0, where t is the displacement of the platen and t_0 is the original thickness of a device. The compressive strain speed was set at 0.35% s^{-1}. The compressive stress was calculated as F/A_0, where F is the force applied to the device and A_0 is the original area of the sample. Pure shear tests were conducted to determine the matrix toughness with a universal testing machine (MTEST-Quattro, ADMET, the loading cell is 150 LB). A rectangular strip of gel (80 × 25 × 4 mm^3) was glued to two rigid acrylate clamps (80 × 10 × 1.5 mm^3). Both unnotched and notched samples were prepared for pure shear tests. For notched samples, an edge crack with a length of 30 mm was cut using a razor blade in the middle section of the sample. The tensile strain rate was fixed at 200% min^{-1}. The tensile strain (ε) was defined as the length change (Δl) divided by the original length (l_0) of the sample. The toughness was defined by integrating the area under a stress–strain curve of the unnotched sample, where strain used the range from 0% to the fractured value of a notched sample.[67] Junction adhesion energy, namely the energy required to increase the unit area of the p–n junction crack, was measured with 180-degree peel tests by the same tensile testing machine. A rectangular strip of DN hydrogel devices (80 × 20 × 4 mm^3) with one end open as an edge crack was used in this peeling test. Both surfaces of a device were bonded to a rigid polyethylene terephthalate (PET) film with super glue, to limit deformation to the crack tip. Two free ends of the device were attached to the machine grips. The loading rate was set constant at 100 mm min^{-1}. The adhesion energy was two times the plateau value of the ratio of the force and width.[68] Mineral oil was used to seal around the whole device to avoid water evaporation during all mechanical tests. Both force and displacement were recorded continuously throughout the experiment.

Optical characterization

The transmittance of AIskin with different thicknesses was measured with a UV-vis spectrometer (SpectraMax M5, Molecular Devices, Sunnyvale, CA) under different humidity conditions.

Electrical characterization

Electrical characterization was conducted both under compressive and tensile modes. The current–voltage characteristics, resistance, open circuit potential, and short circuit current of the as-prepared device were measured by using a source meter (Keithley 2602, Keithley Instrument Inc.) controlled through LabTracer software. The sweep voltage (sweep scan rate = 179 mV s^{-1}) was set at the range from +5 V to −5 V when measuring the rectifying performance. The sweep voltage was set at a constant value of +3 V when measuring the resistance.

The sweep current was set at zero when measuring the open circuit voltage. The sweep voltage was set at zero when measuring the short circuit current. Each compressive/tensile cycle occurred with a 70 s rest during open circuit voltage and short circuit current measurement. The capacitance was measured by using an LCR Meter (Agilent, E4980A) controlled through a LabVIEW interface. In the LCR meter, the test frequency was set at 1 kHz. The resistance and capacitance under various strain rates (2.5% s^{-1}, 5% s^{-1}, 10% s^{-1} and 20% s^{-1}) were studied under compressive mode. Capacitance–voltage (C–V) measurements were performed using an LCR meter under its $C_p - R_p$ mode. The C–V sweeps of the devices were performed between -5 V and 5 V with an AC signal with a peak-to-peak magnitude of 100 mV. In all tests, electrodes were mounted on both the bottom and top of the devices.

Human–machine interface

The four-button touch pad was fabricated by placing 4 pairs of AIskin (12 mm in diameter and 2 mm in thickness) into the VHB spacer with 4 holes. Then the AIskin area was sandwiched between 2 Ag/AgCl electrodes before being sealed by a 3 M transparent tape and another VHB layer. The acquisition of OCV signal from artificial skin to the laptop was realized by an Arduino UNO control board equipped with 10-bit analog-to-digital converters. Python 3.0 was used to analyzed data and program the interface of the greedy snake game.

Statistical analysis

Statistical analyses were performed on GraphPad Prism software (GraphPad Software, Inc.). Results are depicted as mean $\pm$ standard deviation (SD), we conducted an unpaired Student's t test to analyze the statistical differences of experiment results. We used a parametric test and assumed that any experimental groups are normally distributed with the same SD. Differences were considered statistically significant if $P < 0.05$.

Testing of the AIskin on human hands

Informed consent was obtained from the human participant for the experiments.

Conflicts of interest

The authors have no conflict to declare.

Acknowledgements

References

1 J. Dargahi and S. Najarian, *Int. J. Med. Rob. Comput. Assist. Surg.*, 2004, **1**, 23–35.
2 M. L. Hammock, A. Chortos, B. C. K. Tee, J. B. H. Tok and Z. Bao, *Adv. Mater.*, 2013, **25**, 5997–6038.
3 A. Chortos, J. Liu and Z. Bao, *Nat. Mater.*, 2016, **15**, 937–950.
4 M. Boer, E. Duchnik, R. Maleszka and M. Marchlewicz, *Adv. Dermatol. Allergol.*, 2016, **33**, 1–5.
5 W. Yang, V. R. Sherman, B. Gludovatz, E. Schaible, P. Stewart, R. O. Ritchie and M. A. Meyers, *Nat. Commun.*, 2015, **6**, 6649.
6 K. Laden and R. Spitzer, *J. Soc. Cosmet. Chem.*, 1967, **18**, 351–360.
7 Y. Lee, C.-H. Lee and U. Oh, *Mol. Cells*, 2005, **20**, 315–324.
8 Y. Roudaut, A. Lonigro, B. Coste, J. Hao, P. Delmas and M. Crest, *Channels*, 2012, **6**, 234–245.
9 Y. Sun, W. M. Choi, H. Jiang, Y. Y. Huang and J. A. Rogers, *Nat. Nanotechnol.*, 2006, **1**, 201–207.
10 D.-H. Kim, N. Lu, R. Ma, Y.-S. Kim, R.-H. Kim, S. Wang, J. Wu, S. M. Won, H. Tao and A. Islam, *Science*, 2011, **333**, 838–843.
11 D.-H. Kim, N. Lu, R. Ghaffari, Y.-S. Kim, S. P. Lee, L. Xu, J. Wu, R.-H. Kim, J. Song and Z. Liu, *Nat. Mater.*, 2011, **10**, 316–324.
12 D.-H. Kim, J. Song, W. M. Choi, H.-S. Kim, R.-H. Kim, Z. Liu, Y. Y. Huang, K.-C. Hwang, Y.-W. Zhang and J. A. Rogers, *Proc. Natl. Acad. Sci. U. S. A.*, 2008, **105**, 18675–18680.
13 T. Sekitani, H. Nakajima, H. Maeda, T. Fukushima, T. Aida, K. Hata and T. Someya, *Nat. Mater.*, 2009, **8**, 494–499.
14 T. Sekitani, Y. Noguchi, K. Hata, T. Fukushima, T. Aida and T. Someya, *Science*, 2008, **321**, 1468–1472.
15 S. J. Benight, C. Wang, J. B. Tok and Z. Bao, *Prog. Polym. Sci.*, 2013, **38**, 1961–1977.
16 J. Y. Oh, S. Rondeau-Gagné, Y.-C. Chiu, A. Chortos, F. Lissel, G.-J. N. Wang, B. C. Schroeder, T. Kurosawa, J. Lopez and T. Katsumata, *Nature*, 2016, **539**, 411–415.
17 R. Pelrine, R. Kornbluh, Q. Pei and J. Joseph, *Science*, 2000, **287**, 836–839.
18 J. Zang, S. Ryu, N. Pugno, Q. Wang, Q. Tu, M. J. Buehler and X. Zhao, *Nat. Mater.*, 2013, **12**, 321–325.
19 D. J. Lipomi, M. Vosgueritchian, B. C. Tee, S. L. Hellstrom, J. A. Lee, C. H. Fox and Z. Bao, *Nat. Nanotechnol.*, 2011, **6**, 788–792.
20 J. Liang, L. Li, X. Niu, Z. Yu and Q. Pei, *Nat. Photonics*, 2013, **7**, 817–824.
21 H. R. Lee, C. C. Kim and J. Y. Sun, *Adv. Mater.*, 2018, **30**, 1704403.
22 C. Yang and Z. Suo, *Nat. Rev. Mater.*, 2018, **3**, 125–142.
23 J. Y. Sun, C. Keplinger, G. M. Whitesides and Z. Suo, *Adv. Mater.*, 2014, **26**, 7608–7614.
24 Z. Lei and P. Wu, *Nat. Commun.*, 2018, **9**, 1134.
25 C.-C. Kim, H.-H. Lee, K. H. Oh and J.-Y. Sun, *Science*, 2016, **353**, 682–687.
26 Y. C. Lai, J. Deng, R. Liu, Y. C. Hsiao, S. L. Zhang, W. Peng, H. M. Wu, X. Wang and Z. L. Wang, *Adv. Mater.*, 2018, **30**, 1801114.

27 P. Rewatkar and S. Goel, *IEEE Trans. Nanobiosci.*, 2018, **17**, 374–379.

28 N. Mehmood, A. Hariz, S. Templeton and N. H. Voelcker, *Biomed. Eng. Online*, 2015, **14**, 17.

29 E. Gianino, C. Miller and J. Gilmore, *Bioengineering*, 2018, **5**, 51.

30 H. Derakhshandeh, S. S. Kashaf, F. Aghabaglou, I. O. Ghanavati and A. Tamayol, *Trends Biotechnol.*, 2018, **30**, 1259–1274.

31 K. Y. Lee and D. J. Mooney, *Chem. Rev.*, 2001, **101**, 1869–1880.

32 Q. Chen, L. Zhu, C. Zhao, Q. Wang and J. Zheng, *Adv. Mater.*, 2013, **25**, 4171–4176.

33 J. P. Gong, *Soft Matter*, 2010, **6**, 2583–2590.

34 J.-Y. Sun, X. Zhao, W. R. Illeperuma, O. Chaudhuri, K. H. Oh, D. J. Mooney, J. J. Vlassak and Z. Suo, *Nature*, 2012, **489**, 133–136.

35 T. Yamada, Y. Hayamizu, Y. Yamamoto, Y. Yomogida, A. Izadi-Najafabadi, D. N. Futaba and K. Hata, *Nat. Nanotechnol.*, 2011, **6**, 296–301.

36 W. Zhang, X. Zhang, C. Lu, Y. Wang and Y. Deng, *J. Phys. Chem. C*, 2012, **116**, 9227–9234.

37 Y. Zhou, Y. Hou, Q. Li, L. Yang, Y. Cao, K. H. Choi, Q. Wang and Q. Zhang, *Adv. Mater. Technol.*, 2017, **2**, 1700118.

38 S. Z. Bisri, S. Shimizu, M. Nakano and Y. Iwasa, *Adv. Mater.*, 2017, **29**, 1607054.

39 M. Lucia, J. Hernandez-Rojas, C. Leon and I. Martil, *Eur. J. Phys.*, 1993, **14**, 86–89.

40 D. S. Cabral, R. L. Moreno, T. C. Pimenta, L. B. Zoccal and P. C. Crepaldi, *Implementation of Schottky barrier diodes (SBD) in standard CMOS process for biomedical applications*, InTech, Croatia, 2012.

41 O. J. Cayre, S. T. Chang and O. D. Velev, *J. Am. Chem. Soc.*, 2007, **129**, 10801–10806.

42 Y. Bai, B. Chen, F. Xiang, J. Zhou, H. Wang and Z. Suo, *Appl. Phys. Lett.*, 2014, **105**, 151903.

43 Y.-H. Na, Y. Tanaka, Y. Kawauchi, H. Furukawa, T. Sumiyoshi, J. P. Gong and Y. Osada, *Macromolecules*, 2006, **39**, 4641–4645.

44 J. Heikenfeld, A. Jajack, J. Rogers, P. Gutruf, L. Tian, T. Pan, R. Li, M. Khine, J. Kim and J. Wang, *Lab Chip*, 2018, **18**, 217–248.

45 G. Zhao, Y. Zhang, N. Shi, Z. Liu, X. Zhang, M. Wu, C. Pan, H. Liu, L. Li and Z. L. Wang, *Nano Energy*, 2019, **59**, 302–310.

46 X. Pu, M. Liu, X. Chen, J. Sun, C. Du, Y. Zhang, J. Zhai, W. Hu and Z. L. Wang, *Sci. Adv.*, 2017, **3**, e1700015.

47 W. Xu, L. B. Huang, M. C. Wong, L. Chen, G. Bai and J. Hao, *Adv. Energy Mater.*, 2017, **7**, 1601529.

48 F.-R. Fan, L. Lin, G. Zhu, W. Wu, R. Zhang and Z. L. Wang, *Nano Lett.*, 2012, **12**, 3109–3114.

49 N. Yamazoe and Y. Shimizu, *Sens. Actuators*, 1986, **10**, 379–398.

50 G. Wee, O. Larsson, M. Srinivasan, M. Berggren, X. Crispin and S. Mhaisalkar, *Adv. Funct. Mater.*, 2010, **20**, 4344–4350.

51 O. Larsson, E. Said, M. Berggren and X. Crispin, *Adv. Funct. Mater.*, 2009, **19**, 3334–3341.

52 M. Ahmadipour, M. F. Ain and Z. A. Ahmad, *IEEE Sens. J.*, 2017, **17**, 3224–3230.

53 S.-M. Lim, H. Yoo, M.-A. Oh, S. H. Han, H.-R. Lee, T. D. Chung, Y.-C. Joo and J.-Y. Sun, *Proc. Natl. Acad. Sci. U. S. A.*, 2019, 201903900.

54 Y. Hou, Y. Zhou, L. Yang, Q. Li, Y. Zhang, L. Zhu, M. A. Hickner, Q. Zhang and Q. Wang, *Adv. Energy Mater.*, 2017, **7**, 1601983.

55 S. Xu, Y. Qin, C. Xu, Y. Wei, R. Yang and Z. L. Wang, *Nat. Nanotechnol.*, 2010, **5**, 366–373.

56 K. Dong, Y.-C. Wang, J. Deng, Y. Dai, S. L. Zhang, H. Zou, B. Gu, B. Sun and Z. L. Wang, *ACS Nano*, 2017, **11**, 9490–9499.

57 S. Park, H. Kim, M. Vosgueritchian, S. Cheon, H. Kim, J. H. Koo, T. R. Kim, S. Lee, G. Schwartz and H. Chang, *Adv. Mater.*, 2014, **26**, 7324–7332.

58 Y. Wang, Z. Wang, Z. Su and S. Cai, *Extreme Mech. Lett.*, 2019, **28**, 81–86.

59 H. Yuk, T. Zhang, G. A. Parada, X. Liu and X. Zhao, *Nat. Commun.*, 2016, **7**, 12028.

60 Z. Guo, U. Aboudi, P. Peumans, R. T. Howe and F.-K. Chang, *J. Microelectromech. Syst.*, 2016, **25**, 524–532.

61 S. Wang, J. Xu, W. Wang, G.-J. N. Wang, R. Rastak, F. Molina-Lopez, J. W. Chung, S. Niu, V. R. Feig and J. Lopez, *Nature*, 2018, **555**, 83–88.

62 Q. Hua, J. Sun, H. Liu, R. Bao, R. Yu, J. Zhai, C. Pan and Z. L. Wang, *Nat. Commun.*, 2018, **9**, 244.

63 Q. Xu, L. An, M. Yu and S. Wang, *Macromol. Rapid Commun.*, 2008, **29**, 390–395.

64 J. Wu, Z. Wu, S. Han, B.-R. Yang, X. Gui, K. Tao, C. Liu, J. Miao and L. K. Norford, *ACS Appl. Mater. Interfaces*, 2018, **11**, 2364–2373.

65 M. Sun, R. Bai, X. Yang, J. Song, M. Qin, Z. Suo and X. He, *Adv. Mater.*, 2018, **30**, 1804916.

66 J. Kim, J. R. Sempionatto, S. Imani, M. C. Hartel, A. Barfidokht, G. Tang, A. S. Campbell, P. P. Mercier and J. Wang, *Adv. Sci.*, 2018, **5**, 1800880.

67 J. Li, W. R. Illeperuma, Z. Suo and J. J. Vlassak, *ACS Macro Lett.*, 2014, **3**, 520–523.

68 R. Rivlin and A. G. Thomas, *J. Polym. Sci.*, 1953, **10**, 291–318.